Measuring thickness of marine ice using IR thermography

Taimur Rashid, Hassan Abbas Khawaja, Kåre Edvardsen

PII: S0165-232X(18)30209-X
DOI: doi:10.1016/j.coldregions.2018.08.025
Reference: COLTEC 2654

To appear in: *Cold Regions Science and Technology*

Received date: 8 May 2018
Revised date: 10 July 2018
Accepted date: 23 August 2018

Please cite this article as: Taimur Rashid, Hassan Abbas Khawaja, Kåre Edvardsen , Measuring thickness of marine ice using IR thermography. Coltec (2018), doi:10.1016/j.coldregions.2018.08.025

Measuring Thickness of Marine Ice Using IR Thermography

Taimur Rashid*, Hassan Abbas Khawaja, Kåre Edvardsen

UiT-The Arctic University of Norway, Hansine Hansens veg 18, 9019, Tromsø, Norway

Abstract

There are several challenges to operating in a cold climate. Marine icing is one of them, and its mitigation is vital for marine operations.

The presented work is a laboratory-scale setup to measure marine ice thickness. The developed methodology can be applied towards de-/anti-icing setups. The method described is based on measuring the average surface temperatures of the marine ice. Infrared thermography (IRT) is used to measure the thermal response of ice when subjected to active heating. These tests are performed at various controlled climatic conditions. The surface temperature profiles of marine icing samples are recorded with a calibrated high definition infrared camera. The results show distinct thermal profiles for different ice thicknesses (5, 10 and 15mm).

The thermal profile revealed three parameters, namely: time to respond (t_0), rate of change of temperature $\left(\frac{\partial T}{\partial t}\right)$, and time to reach ΔT of 5°C (t_f). These parameters can be empirically correlated to initial temperature (T_0) and ice thickness (t_h). It was found that time to respond (t_0) had a strong correlation with ice thickness (t_h); however, the rate of change of temperature $\left(\frac{\partial T}{\partial t}\right)$ and time to reach ΔT of 5°C (t_f) were both dependent on initial temperature (T_0) and ice thickness (t_h).

The study mentioned above is conceptual proof that ice thickness can be measured with the given setup, taking into account environmental parameters and accurate calibration.

Keywords: marine ice, ice thickness, infrared imaging, thermography, marine operations, cold climate

1. Introduction

A. Cold Climate Operations

Cold climate operations face several challenges. Recent activity in the Arctic Circle has encouraged researchers to study the various challenges. One of these is marine icing phenomenon. The long-term exposure of the superstructures to marine icing can cause rapid ice accretion, which can be hazardous for both human and machine safety (Makkonen, 1984, Ryerson, 2011, Shellard, 1974, Ayele and Barabadi, 2016). The uncertainty in the prediction of icing makes this issue all the more significant.

Icing on ships and offshore structures is caused by atmospheric sources and sea spray, with sea spray being the major contributor to icing. It is generated by the collision of sea waves, the breaking of waves due to strong winds and bursting bubbles that float upon the waves (Lozowski E.P, 2000, C.D O'Dowd, 2008, Rashid et al., 2016b). The droplets produced from the sea spray travel at a certain trajectory and fall upon different parts of ships such as rails, deck, stairs, etc. These droplets freeze, typically during their trajectory path, due to the low atmospheric temperature (Samuelsen et al., 2017, Stallabrass, 1980). The droplets are known as sea spray, which is the main source of marine icing on various parts of ships (Stallabrass, 1980). Generally, sea spray icing occurs at the lower heights of the ship's surface such as decks, derricks and handrails. The height of the sea spray is approximately 16 m above sea level (Sultana et al., 2018, WMO, 1962).

Various empirical models have been developed to predict the marine icing phenomenon. Many of these models are based on the extensive icing data collected between the 1960s and 1980s and are reported by researchers (Brown and Roebber, 1985, Overland et al., 1986, Roebber and Mitten, 1987, Samuelsen et al., 2017, Stallabrass, 1980, Zakrzewski et al., 1989). This study has gained momentum over the past 20 years. Researchers have come up with

empirical relationships, including different parameters, to explain and accurately predict marine icing phenomenon, e.g.(Dehghani-Sanij et al., 2017, Samuelsen et al., 2017) These parameters include atmospheric temperature, wind speed, droplets' mass, droplets' travel time, etc. Dehghani et al. (2017) have developed an analytical model for heat conduction through brine-spongy ice, and Fazelpour et al. (2017) have demonstrated an image-processing method to detect accumulated ice on known structures.

B. Significance of Ice Mitigation

Marine icing can accrete on the ship's structure rapidly, causing a potential safety hazard. The time taken to mitigate this risk is essential for the equipment and personal safety. With the introduction of the Polar Code in 2017 by the International Maritime Organization (IMO), ships must be classified according to a certain polar category, in order to operate in the cold climate region (IMO, 2016). The Polar Code has been implemented to minimize the risks to shipping operations in cold climates. Currently, various methods are being used to remove icing (de/icing) on ships. These involve electrical, mechanical, chemical and manual methods (Ryerson, 2009, Rashid et al., 2016b). Once marine icing has accreted on the ships, more energy is required to remove it. Consequently, if ice mitigation is performed prior to the marine icing phenomenon, it could save more energy and time.

C. Infrared Thermography

Infrared thermography is the use of the electromagnetic radiation intensity emitted by an object in the infrared spectral region from 0.75mm to 1000mm (Gaussorgues, 1994). This emitted radiations can be visualized using false colours. The radiation characteristics of the objects can be understood by a *blackbody*. This is an ideal theoretical body, which absorbs all the incident radiation without any transmission and reflection. The blackbody is a perfect absorber or emitter at all electromagnetic wavelengths (Grum and Becherer, 1979). However,

in the real world, we deal with objects having the ability to emit, absorb and radiate energy. This can be described by Kirchhoff's law, as shown in Equation (1),

$$\alpha\lambda + \varphi\lambda + \tau\lambda = 1 \quad (1)$$

where α is the coefficient of energy absorbed, φ is the coefficient of energy reflected and τ is the coefficient of energy transmitted.

The emissivity ε (dimensionless) is defined as the ratio between the radiant flux exiting the true radiating body M_r (W/m^2) and an ideal blackbody M_b (W/m^2) at the same temperature as shown in Equation (2).

$$\varepsilon = {M_r}/{M_b} \quad (2)$$

The emissivity is defined on the scale of 0 to 1, with zero being the least emissive and 1 being a perfect emissive (blackbody).

In addition, most materials are opaque to the infrared camera; i.e. the transmission factor can be considered zero ($\tau\lambda = 0$). Hence, Equation (1) can be simplified to Equation (3).

$$\epsilon\lambda + \varphi\lambda = 1 \quad (3)$$

The IR spectral region is generally divided into four sub-regions: near infrared (NIR) from 0.7 to 1μm, shortwave infrared (SWIR) from 0.9 to 2.5μm, mediumwave infrared (MWIR) 2 to 5μm and longwave infrared (LWIR) 8 to 14μm.

The thermographic operating range of an infrared (IR) camera can be categorized in two broad ranges. One spectral range is from 2 to 5μm, referred to as the SW/MWIR band. The other IR range is from 8 to 14μm, referred to as the LWIR band. Most commercial thermographic cameras are based on these two bands. The temperature measurement carried out by most IR cameras is based on the intensity of the photons striking the surface of the detectors. This can be explained by Planck's law, as shown in Equation (4).

$$U_{\lambda,b}(\lambda,T) = \frac{2hc^2}{\lambda^5(e^{hc/\lambda kT})-1}\ x\ 10^6\ [W/m^2(\mu m)] \quad (4)$$

where $U_{\lambda,b}$ is the blackbody's spectral radiant emittance at wavelength λ (m), c is the velocity of light (2.99 x 10^8 m/s), h is Planck's constant (6.6 x 10^{-24} joules/sec), k is Boltzmann's constant (1.4 x 10^{-23} joule/K) and T is the absolute temperature of the blackbody (K).

The spectral distribution (Planck curves) of the blackbody's radiant energy over different wavelengths and surface temperatures is shown in Figure 1. This demonstrates that the longwave IR range is suitable for cold objects' thermography. The Planck curves for the blackbody emission are shown in Figure 1. The ice emissivity varies from 0.965 to 0.995 in the range of 4μm to 13μm wavelengths, which means that ice has high radiative emittance in the LWIR range (Zhang, 1999, Khawaja et al., 2016). An LWIR camera was used in our experiment.

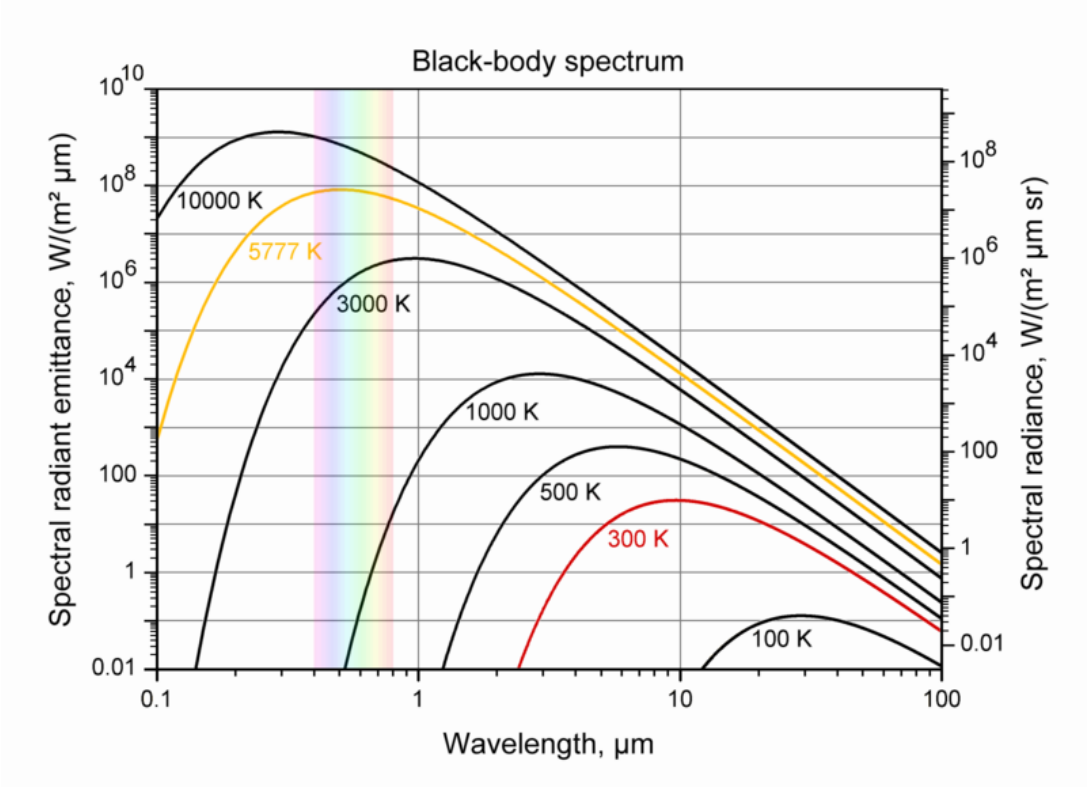

Figure 1: Planck curves for a blackbody at various temperatures

IR thermography has been used to observe icing, which includes snow grains, freezing lakes, pure and saline ice, as reported by (Barber et al., 2014, Hori et al., 2013, Rashid et al., 2015, Shea and Jamieson, 2011). The advantages of using IR thermography include larger area of detection, non-destructive testing, non-contact measurement and ease of data collection. In a recent study (Rashid et al., 2016a), passive IR thermography was successfully used to observe thermal gradients on the surface of a saline ice sample. The studies also suggest improvements in thermographic techniques to measure additional parameters of ice such as thickness.

2. Methodology

Marine ice thickness is determined by measuring the surface temperature of the marine icing samples. This is performed by applying heat energy to an icing sample for a certain period of time. The surface temperature of the icing sample is monitored during this period. The heat energy is supplied underneath the icing sample, using a heating source that is directly in contact with the icing sample. Initially, the icing sample and the heating source are kept at thermal equilibrium state. As soon as heat energy is supplied from a heating source, a thermal non-equilibrium state is created. In order to attain a thermal equilibrium state, the heat energy is transmitted from the heating source to the icing sample. This is a typical heat transfer phenomenon between the two physical masses, which are in contact and possess a non-equilibrium thermal state. The heat transfer process in a three-dimensional space can be expressed by the heat equation shown in Equation (4) (Moran, 2003),

$$\frac{\partial T}{\partial t} = k\left(\frac{\partial^2 T}{\partial x^2} + \frac{\partial^2 T}{\partial y^2} + \frac{\partial^2 T}{\partial z^2}\right) \tag{4}$$

where T is the temperature (K), k is the thermal diffusivity constant (W/m^2), x, y, z are the spatial dimensions and t is the time (sec).

The heat transfer process causes a temperature distribution within the icing sample. The temperature distribution within the icing sample is $T\ (x, t)$, with x a spatial coordinate and t being time (sec). The marine icing sample is enclosed in an aluminium container with an open top surface, as shown in Figure 5. The heat energy is supplied to the icing sample from underneath. As a result, the surface temperature is changed, due to the heat transfer occurring

from the bottom to the top of the icing surface, which is the focus of our study. The change in surface temperature (ΔT) of the icing sample is due to the one-dimensional heat flow. The one-dimensional heat transfer can be expressed by the heat equation shown in Equation (5),

$$\frac{\partial}{\partial x}\left(k\frac{\partial T}{\partial x}\right) + \dot{q} = \rho c \frac{\partial T}{\partial t} \tag{5}$$

where T is the temperature (K), x is the spatial position m, t is the time (sec), ρ is the density of the medium (kg/m3), c is the specific heat capacity (J/(kg K)), $\dot{q}$ is the volumetric energy generation term (W/m3) and k is the coefficient of thermal conductivity ($\frac{W}{m}.K$)).

The mode of heat transfer between the two solid mediums (heating source and the icing sample) is conduction. This process can be described in terms of an appropriate rate equation, describing the amount of energy being transferred per unit time (heat flux). The rate equation for the conduction is known as Fourier's law, and the heat flux $q_x^{"}$ (W/m^2) in a single dimension with temperature distribution $T(x)$ can be expressed as Equation (6).

$$q_x^{"} = -k\,\frac{dT}{dx} \tag{6}$$

The temperature distribution ($\frac{dT}{dx}$) within the icing sample is due to the conditions occurring at the boundaries; i.e., the point of contact of the icing samples with the metallic plate of the heating source is shown in Figure 2. The conduction process in the icing sample is determined by the temperature distribution within the icing samples. Figure 2 explains the relationship between the heat flux($q_x^{"}$), temperature distribution $\frac{dT}{dx}$ and a single-dimensional coordinate system (x-axis) of an icing sample.

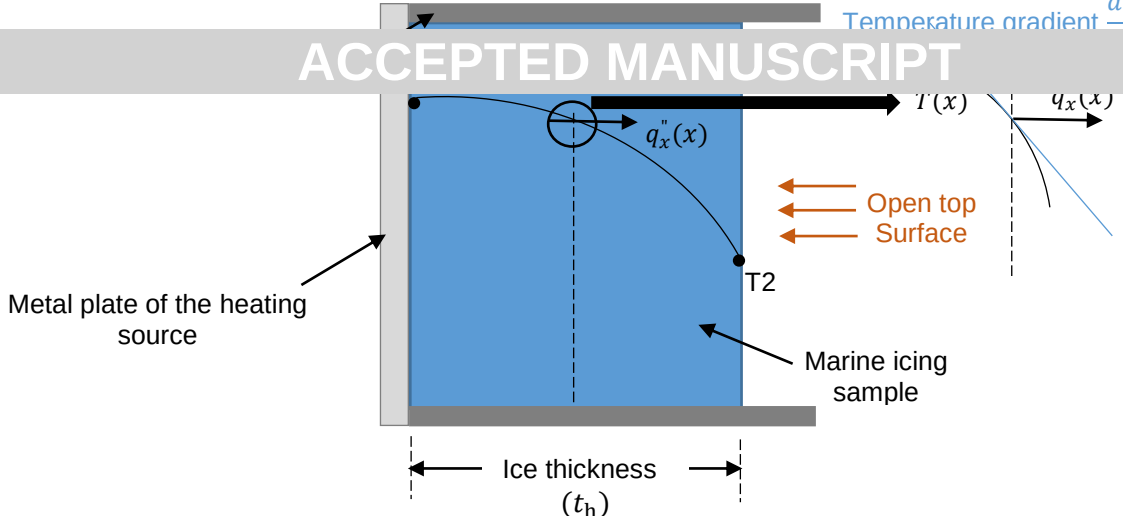

Figure 2: Relationship between heat flux, temperature gradient and coordinate system within an icing sample (adapted from (Moran, 2003))

Provided the boundary conditions are similar, the temperature distribution $(\frac{dT}{dx})$ will change within the icing sample for different thicknesses (t_h). This is due to a change in thermal diffusion (K). As a result, the temperature (T_2) at the surface of the icing sample will vary. We have analysed the surface temperature (T_2) of marine icing samples having different thicknesses $(t_{h1}, t_{h2}$ ...). For comparison purposes, similar temperatures (T_1) and environmental conditions are provided for the icing samples.

The thickness (t_h) of the marine icing sample was evaluated in a laboratory-scale experimentation. The thickness levels of the marine icing samples were analysed as a function of surface temperature gradient ΔT (C^o) and time t (sec), as shown in Equation (7).

$$t_h = f(\Delta T, t) \tag{7}$$

The infrared camera was used to measure the surface temperature gradient (ΔT) of the marine icing samples. The infrared camera measures the changes in surface temperature by capturing its radiation intensity, as described in Equation (3).

A. Experimental Setup

A laboratory-scale experimental setup was prepared, to measure different ice thickness samples. These icing samples were prepared from sea water. The experimental setup consisted of the following components.

LWIR Camera

The FLIR® T1030Sc camera was used for thermographic imaging in the experimentation, as shown in Figure 2. The IR spectral range of this camera is between 7-12um (LWIR), with a detector type of an uncooled microbolometer. The pixel resolution of the T1030Sc camera is 1024 x 768 pixels, with thermal sensitivity of less than 20mK at +30°C (+86°F).

Cold Room Chamber

The cold room chamber at The Arctic University of Norway was used to freeze the ice samples. The cold room has the capacity to provide a low-temperature environment of up to -40°C. However, due to the operational limitations of its cooling system, all observations were recorded below -20°C. The humidity level of the cold room was kept low, to avoid icing over the compressor blades.

Environmental Test Chamber

The environmental test chamber was used to monitor the ice samples, as shown in Figure 5. The temperature of this test chamber is adjustable up to -50°C. The test chamber has the provision of a monitoring window and cable opening on its side wall. This opening is used for the necessary cables running inside the test chamber.

Ice Containers

Small-sized ice containers were fabricated to freeze the marine icing samples, as shown in Figure 2. These ice containers were machined from aluminium sheet, using an industrial standard lathe machine. The dimensions of an icing container are 2.1cm x 2.1cm x 2cm. The bottom surface of the container was glued to the metal base of the heating element. It was then sealed with a commercial water proofing sealant. The container can hold marine water at the desired level without any leakage. The top surface of the icing container was kept open.

Hardware Control Unit

A hardware control unit with customized circuitry was used to control the infrared red camera and heating elements, simultaneously. This hardware circuitry was connected to the universal serial bus data acquisition module, namely USB-6009 from National Instruments®. The heating elements were controlled from data acquisition module software. The heating elements were turned on and off periodically to provide the required heating to the icing samples.

The hardware control unit communicates with the customized software user interface. The software of the user interface was developed using MATLAB®. This software user interface provides communication protocols to the hardware control unit and the infrared camera. The communication protocols were developed using a software development kit (SDK) of MATLAB®, namely *FLIR® Atlas SDK*. In addition, the interface uses the National Instruments'® session-based program to control the digital output channels of NI USB-6009.

FLIR ®T1030sc LWIR Camera

Icing Container

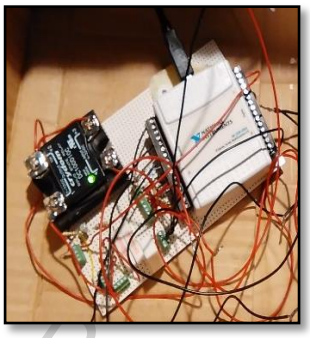

Hardware Control Unit

Cold Room

Tenney Jr. Environmental Chamber

Figure 3: Setup components

The experimentation process is shown in Figure 4. The marine icing samples were prepared by freezing sea water in the icing container. The sea water was collected from Norskhavet (GPS 69°41'07.2"N 19°00'23.3"E). Controlled laboratory tests were performed to measure the salinity of the sea water sample used for experimentation. The salinity of seawater is 46.4±0.9 g/l. The icing container was attached to the flat plate of the heating element. The top surface of the icing container was exposed, to measure the surface temperature of the icing sample. Icing samples of different thicknesses, such as 5mm, 10mm and 15mm, were frozen inside the icing containers. Positive temperature coefficient (PTC) resistive heating elements were used to provide heating to the icing samples. There was direct contact between the icing samples and the plate of the heating element. The walls of the icing container provided thermal insulation of the heating elements from all sides, excluding the top surface. Hence, the maximum possible heat transfer was allowed from the top surface of the heating elements.

The icing samples were taken out of the cold room and put inside the cold box, along with the hardware control unit. Inside the cold box, the temperature is adjustable up to -55^{o}C. The experimentation was performed at different negative temperatures inside the cold box from -15^{o}C to -30^{o}C. The infrared camera was mounted on a stand at an angle of 90° to observe the thermal behaviour of the icing samples in the containers when heated from underneath.

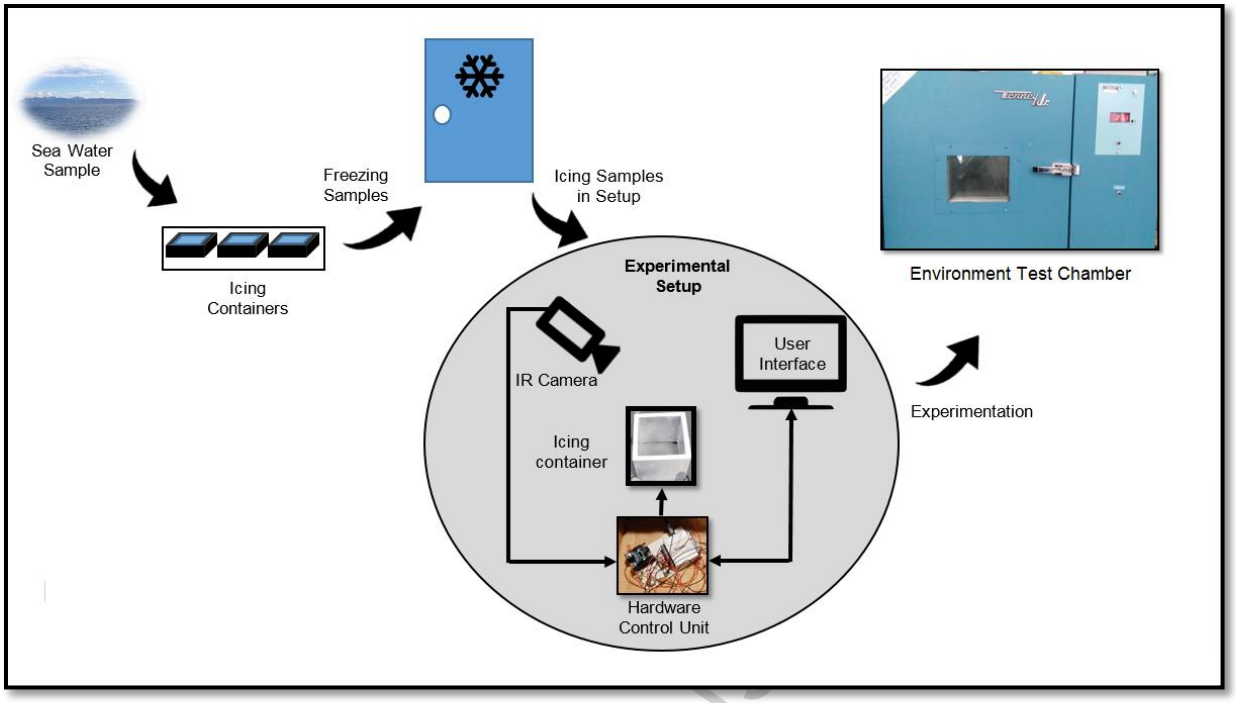

Figure 4: Experimentation process

B. Operating Cycle

The operating cycle (Figure 4) of the experimentation started from taking out the icing containers from the freezer. The icing containers and the hardware control unit were placed inside the cold box. The temperature inside the cold box was adjusted to a specific freezing temperature. The icing samples were heated by turning on the heating elements. The infrared images were recorded simultaneously, using the software user interface panel. The average surface temperature profiles were recorded at the frame rate of 10Hz). The temperature data was recorded in a log file with time stamps. After a certain period of time, the heating elements were switched off, completing the operating cycle.

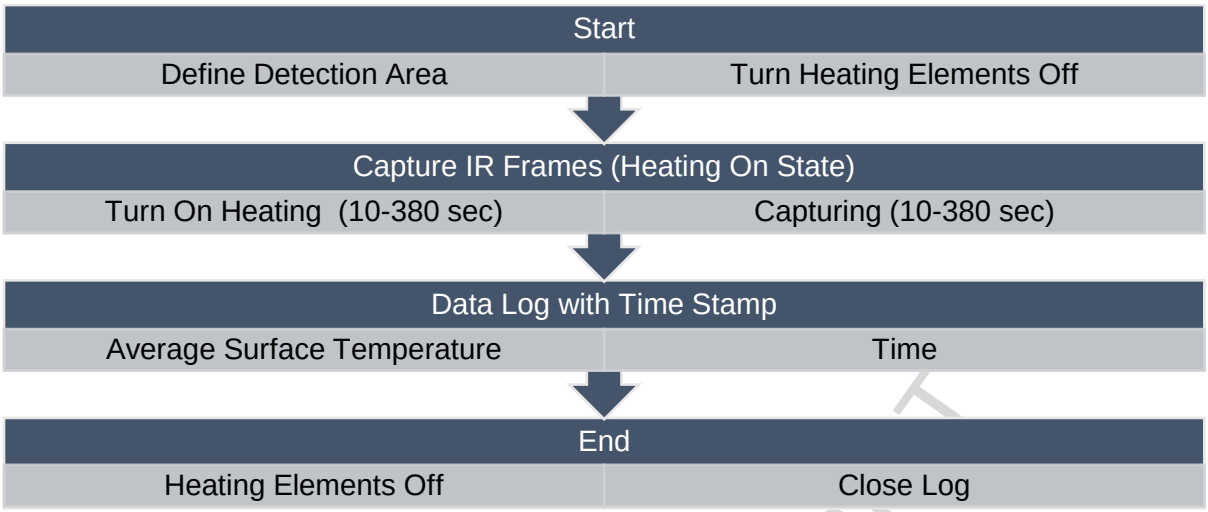

Figure 5: Operating cycle

The analytical demonstration related to the experimental work is presented in the study by Khawaja et al. (2016). This study shows numerical methodologies to simulate the three-dimensional IR signature of an ice cube. The thermal conductivity of the seawater ice sample prepared in our work is demonstrated and verified by Rashid et al. (2016). In this work, the thermal conductivity of the seawater ice is calculated using IR thermography, and analytical simulations verify the IR measurements.

3. Results and Discussion

The average surface temperature of the ice samples showed a particular response when heated inside the cold environment. This particular response (shown in Figure 6) can be acquired by plotting the average surface temperature (T) of the ice against time. Figure 6 shows three parameters of interest. One is the time (t_0) required to the first significant change in temperature with respect to the starting temperature (T_o). It is the time calculated immediately after the heating was turned on until the surface temperature of the ice started to rise. The second parameter is the rate of change in surface temperature $\left(\frac{\partial T}{\partial t}\right)$ of the ice. The third parameter is the time (t_f) taken by the ice sample to reach $\Delta T = 5°C$. We observed that all these parameters represented a distinct response for different ice thicknesses(t_h).

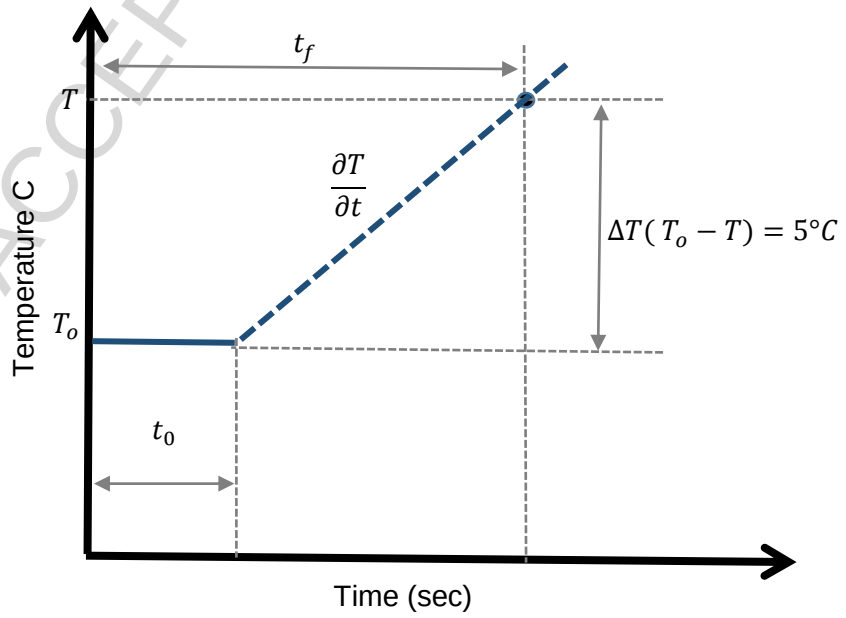

Figure 6: Thermal response of ice surface during heating

Three ice samples' thicknesses are selected for comparison (5mm, 10mm and 15mm), as shown in Figure 7. They have a total volume of 2.2cm^3, 4.4 cm^3, and 7.2 cm^3, respectively. These samples were tested for thickness at three different initial temperatures (T_o) such as -20°C, -25°C and -30°C. Plots of the average surface temperatures against the elapsed time are provided in Figure 8, Figure 9, and Figure 10. The parameters T_o, t_0, and t_f are highlighted in these plots.

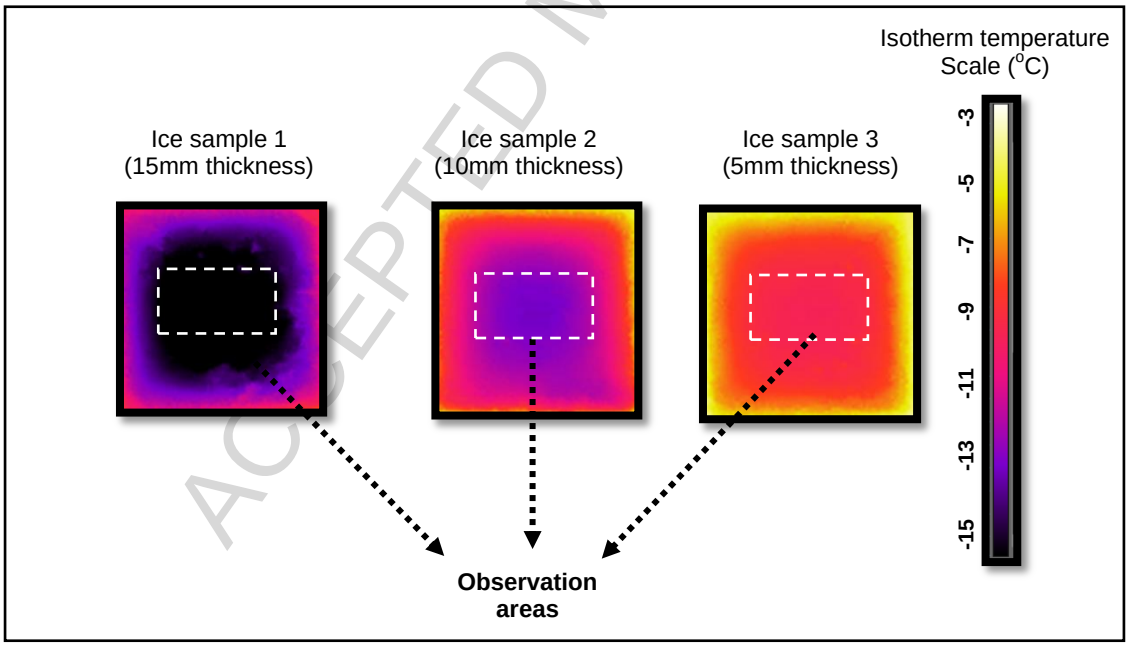

Figure 7: IR images of the surface area of the ice samples

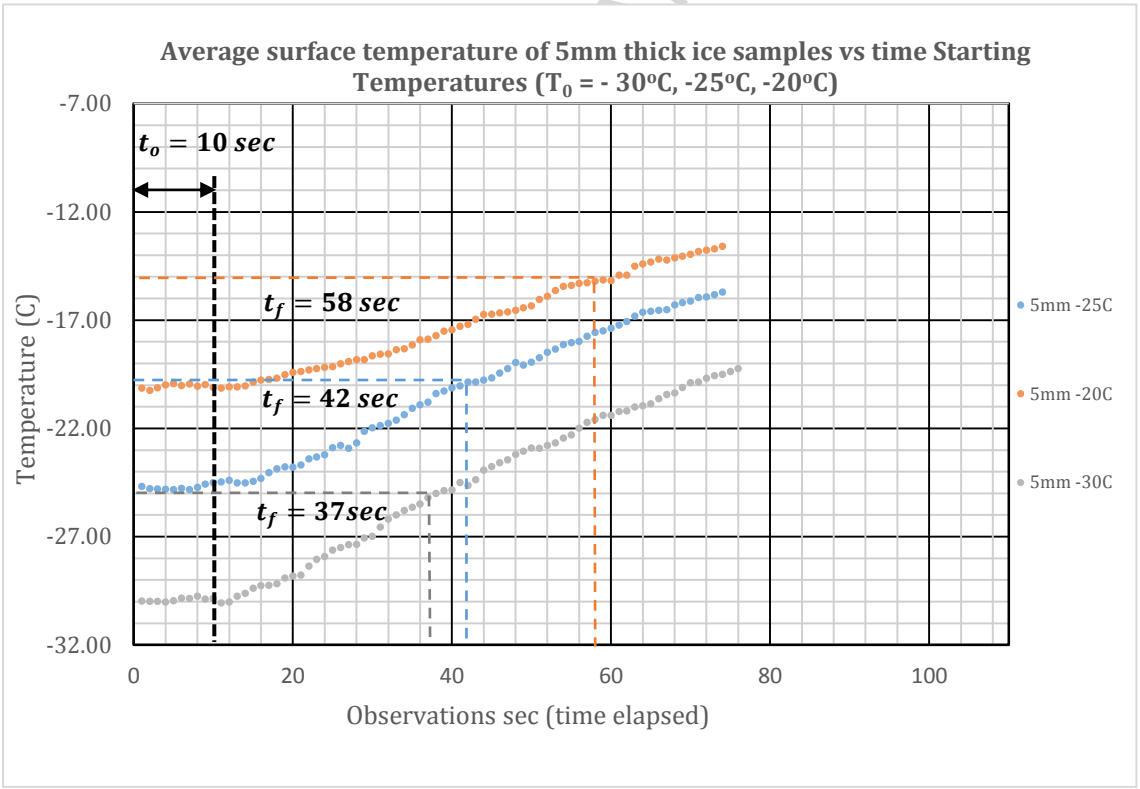

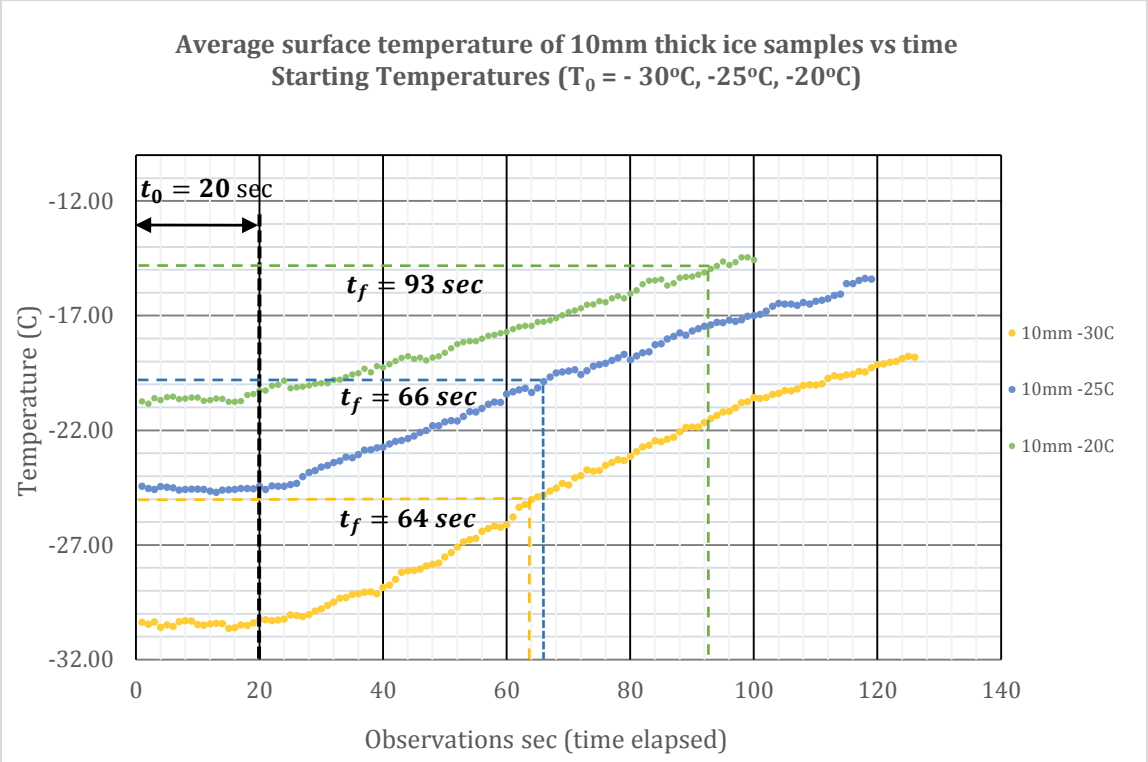

Figure 8: Average surface temperature profiles of ice samples (t_h = 5mm), when subjected to heating at different starting temperatures (T_o)

Figure 9: Average surface temperature profiles of marine icing samples (t_h =10mm), when subjected to heating at different starting temperatures

Figure 10: Average surface temperature profiles of marine icing samples (t_h =15mm), when subjected to heating at different starting temperatures

Table 1 shows a summary of the parameters listed in Figure 6. It presents the numerical values for time to respond (t_0), rate of change in surface temperature $\left(\frac{\partial T}{\partial t}\right)$ of ice and time (t_f) taken by the ice to reach $\Delta T = 5°C$. The values of these parameters are concluded from Figure 8, Figure 9 and Figure 10. These parameters can be empirically correlated with the ice thickness (t_h). For instance, one of the key results indicates that the time to respond (t_0) for a particular ice thickness has a specific value. This value remains unchanged when

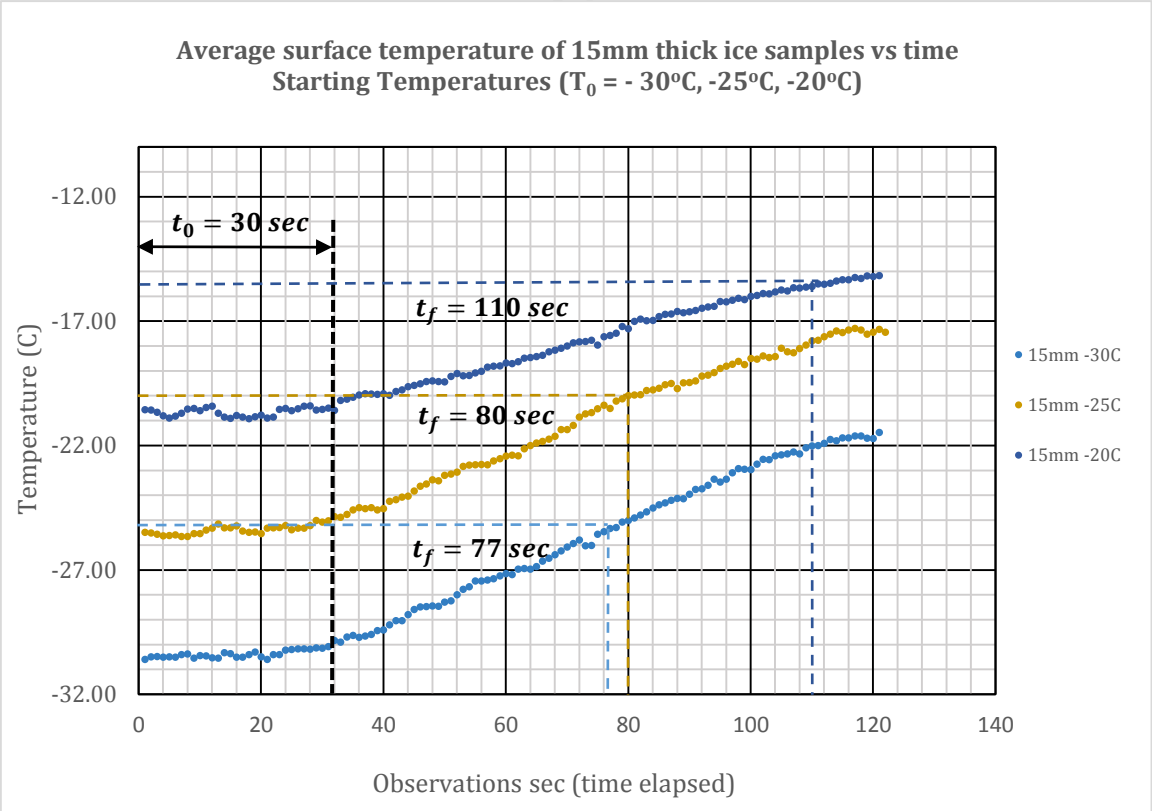

the specific ice is heated at different initial temperatures (T_o). Figure 8, Figure and Figure 10

show that time to respond (t_0) gives a significant indication for measuring the thickness of the ice.

Table 1: The values of $(t_0), (t_f), (\frac{\partial T}{\partial t})$ measured inside a cold environment at different initial temperatures $(T_o = -20°C, -25°C, -30°C)$

Initial Temperature $T_o = -20°C$			
Ice thickness $(t_h)mm$	Rate of change in surface temperature $(\frac{\partial T}{\partial t})\,°C/\text{sec}$	Time to reach $\Delta T = 5°C$ $(t_f)\ sec$	Time to rise $(t_0)\ sec$ $t_o \approx t_f - \frac{5}{(\frac{\partial T}{\partial t})}$
5	0.104	58	10
10	0.068	93	20
15	0.062	110	30
Initial Temperature $T_o = -25°C$			
Ice thickness $(t_h)mm$	Rate of change in surface temperature $(\frac{\partial T}{\partial t})\,°C/\text{sec}$	Time to reach $\Delta T = 5°C$ $(t_f)\ sec$	Time to rise $(t_0)\ sec$ $t_o \approx t_f - \frac{5}{(\frac{\partial T}{\partial t})}$
5	0.156	42	10
10	0.109	66	20
15	0.1	80	30
Initial Temperature $T_o = -30°C$			

Ice thickness $(t_h)mm$	Rate of change in surface temperature $(\frac{\partial T}{\partial t})\,°C/\text{sec}$	Time to reach $\Delta T = 5°C$ $(t_f)\ sec$	Time to rise $(t_0)\ sec$ $t_o \approx t_f - \frac{5}{(\frac{\partial T}{\partial t})}$
5	0.185	37	10
10	0.113	64	20
15	0.106	77	30

The time required to respond (t_0) increases with its thickness (t_h). Table 1 shows that the time (t_0) taken for 15mm is greater (15 seconds), compared to 10mm- and 5mm-thick ice (10 seconds and 5 seconds, respectively). It is observed to be independent of the starting temperatures (T_o).

The rate of change in the surface temperature of ice $\left(\frac{\partial T}{\partial t}\right)$ decreases with its thickness (t_h), as shown in Table 1. For instance, there is a rapid rise in surface temperature of 5mm-thick ice, compared to 10mm- and 15mm-thick ice. Considering a specific ice thickness, the rate of change in temperature $\left(\frac{\partial T}{\partial t}\right)$ varies with different starting temperatures. For instance, $(\frac{\partial T}{\partial t})$ of 10mm ice at (T_o) of $-20°C$ is different, compared to when (T_o) is $-25°C$ and $-30°C$. Similar behaviour can be observed for the 5mm- and 15mm-thick ice.

Table 1 also shows the values of time (t_f) taken by the ice to reach a five-degree rise in temperature $(\Delta T = 5°C)$. A direct relationship can be observed between t_f and the ice

thickness (t_h) at a specific initial temperature (T_o). The time (t_f) increases with the increase in ice thickness (t_h). For instance, t_f calculated for a 5mm-thick ice sample is 58 seconds (at $T_o = -20°C$). This value (t_f) is less than that of the 10mm- and 15mm-thick ice ($t_f = 93\ sec\ and\ t_f = 110\ sec$), respectively. The rest of the (t_f) values in Table 1 show similar behaviour to that discussed. Considering the variable (T_o), we observe an increase in time (t_f) with a decrease in starting temperatures (T_o) for a specific ice thickness (t_h). For instance, the time (t_f) taken by 5mm-thick ice is 37 seconds at the $T_o = -20°C$, while at -25°C and -30°C, t_f is greater, i.e. 42 seconds and 58 seconds, respectively.

Table 2 summarizes the relationship between the correlated parameters. The time (t_0, t_f) and rate of temperature change $\left(\frac{\partial T}{\partial t}\right)$ respond to ice thickness in a specific manner, as described in the discussion above. We observed that (t_0) is the reliable parameter for detecting ice thickness. This is because (t_0) is the time when heat transfer is only happening through the metal surface, adhesive and ice. Essentially, it is due to conduction and is highly predictable, regardless of the environmental conditions. Hence, (t_0) could be a direct means to measure ice thickness. However, (t_0) would be non-linear if ice thickness is considerably large and the initial temperature (T_o) is close to the freezing temperatures. The reason for this is the phase change of the ice surface that is in touch with the heating (i.e. ice melts at the heater contact).

The rate of temperature change $(\frac{\partial T}{\partial t})$ is not solely dependent on the conduction phenomenon. It is also dependent on convection on the ice surface. From the heat transfer point of view, $(\frac{\partial T}{\partial t})$ would be non-linear to ice thickness, mainly due to convection. In addition, it will be dependent on the environmental conditions.

The time (t_f) for a five-degree (Celsius) rise $(\Delta T = 5°C)$ is an integral effect of conduction and convection. Similar to $(\frac{\partial T}{\partial t})$, (t_f) would also be non-linear and dependent on the environmental conditions. If (T_o) is not low enough then it would record the effect of phase change (ice melts at the heater contact).

Table 2: Correlation matrix of ice thickness (t_h) with time to respond (t_0), time to reach $\Delta T = 5°C$ (t_f) and rate of change in surface temperature $(\frac{\partial T}{\partial t})$

Variable	**Correlated Parameters**				
	t_0	$t_f{}^*$	$\frac{\partial T^*}{\partial t}$		T_0
t_h	**D**	**D**	**I**	**N**	**x**
T_0 (for specific t_h)	**x**	**I**	**I**	**N**	**-**

x = Independent or Weak Relationship D = Direct Relationship

I = Inverse Relationship N= Nonlinear

**subject to environmental conditions*

The laboratory setup can be implemented in a real-time scenario by installing individual heating elements underneath a large surface. These heating elements have to be individually controlled by the hardware setup and monitored by the IR camera. The operating cycle shown in Figure 1 is executed whenever the ice thickness information is required. The parameters t_0, $\frac{\partial T}{\partial t}$ and t_f are calculated for the surface area above each heating element. Consequently, an

ice thickness map can be created for the observed surface. This could lead to identification of surface areas that need to be ice-free.

In a real-time scenario, the parameters $t_0, \frac{\partial T}{\partial t}$ and t_f are computed from IRT, which can slightly vary from the findings of our laboratory experimentation. In that case, a spot calibration setup will be required which can be extended to a surface area. The calibration will depend upon the salinity of the ice, the viewing angle of the installed IR camera, and the installation/thermal specifications of the heating elements and the insulating materials placed underneath. The parameters $t_0, \frac{\partial T}{\partial t}$ and t_f obtained from the spot calibration setup can assist in identifying correct information about ice thickness levels.

The presented methodology has an application regarding efficient anti/de-icing. To date, there are no reports of anti/de-icing systems that are based on marine ice thickness. The presented setup uses a non-contact, remote monitoring method that can be implemented on a larger platform, to determine the ice thickness.

4 Conclusion

This paper has discussed the mechanism for measuring the thickness of marine ice with infrared thermography. A laboratory-scale setup was prepared to observe the thermal behaviour of the ice. The ice samples were prepared by freezing sea water of different thickness levels. These were frozen at different temperatures, ranging from -20°C to -30°C. The ice was provided with constant heating underneath, and temperature gradients were observed on their surfaces for a certain period of time inside a cold environment. The results showed distinguishable temperature profiles with different thicknesses of ice. In these temperature profiles, three parameters were identified which can be correlated with ice thickness: the time to respond (t_0), the time taken by the ice to reach a certain temperature (t_f) and the rate of change of surface temperature ($\frac{\partial T}{\partial t}$). For different initial temperatures, the time to respond (t_0) was observed to be unique for a specific thickness of the ice. This parameter is independent of the initial temperature and provides an indication about the thickness of the icing sample. The methodology presented in the paper requires less time (120-180 seconds) to indicate the ice thickness levels. Hence, this methodology can be applied for detecting marine ice thickness. It can contribute to automated anti-icing/de-icing systems to remove and/or mitigate marine icing on ships and superstructures operating in a cold climate.

Acknowledgement

The authors would like to acknowledge the support of Linda March from The Good English Company, UK for proofreading this work.

Funding

The work reported in this paper is funded by Norges forskningsråd, project no. 195153/160, in collaboration with Faroe Petroleum.

References

AYELE, Y. Z. & BARABADI, A. Risk based inspection of offshore topsides static mechanical equipment in Arctic conditions. 2016 IEEE International Conference on Industrial Engineering and Engineering Management (IEEM), 4-7 Dec. 2016 2016. 501-506.

BARBER, D., EHN, J., PUĆKO, M., RYSGAARD, S., DEMING, J., BOWMAN, J., PAPAKYRIAKOU, T., GALLEY, R. & SØGAARD, D. 2014. Frost flowers on young Arctic sea ice: The climatic, chemical, and microbial significance of an emerging ice type. *Journal of Geophysical Research: Atmospheres,* 119.

BROWN, R. D. & ROEBBER, P. 1985. The ice accretion problem in Canadian waters related to offshore energy and transportation. Downsview, Ontario: Canadian Climate Centre.

C.D O'DOWD, B. L., S. VARGHESE, C. SCANNELL, D. CEBURNIS, M.C FACCHINI 2008. A combined organic-inorganic sea-spray source function. *Geophys Res Lett*.

DEHGHANI-SANIJ, A. R., DEHGHANI, S. R., NATERER, G. F. & MUZYCHKA, Y. S. 2017. Marine icing phenomena on vessels and offshore structures: Prediction and analysis. *Ocean Engineering,* 143**,** 1-23.

DEHGHANI, S., NATERER, G. & MUZYCHKA, Y. 2017. Transient heat conduction through a substrate of brine-spongy ice. *Heat and Mass Transfer,* 53**,** 2719-2729.

FAZELPOUR, A., DEHGHANI, S. R., MASEK, V. & MUZYCHKA, Y. S. 2017. Ice Load Measurements on Known Structures Using Image Processing Methods. *World Academy of Science, Engineering and Technology, International Journal of Electrical, Computer, Energetic, Electronic and Communication Engineering,* 11**,** 907-910.

GAUSSORGUES, G. C., S. 1994. *Infrared thermography,* Chapman and Hall.

GRUM, F. & BECHERER, R. J. 1979. *Optical radiation measurements: Volume 1-Radiometry,* New York, Academic Press, Inc.

HORI, M., AOKI, T., TANIKAWA, T., HACHIKUBO, A., SUGIURA, K., KUCHIKI, K. & NIWANO, M. 2013. Modeling angular-dependent spectral emissivity of snow and ice in the thermal infrared atmospheric window. *Applied optics,* 52**,** 7243-7255.

IMO 2016. International code of safety for ships operating in polar waters (polar code). London, UK: International Maritime Organization.

KHAWAJA, H., RASHID, T., EIKSUND, O., BRODAL, E. & EDVARDSEN, K. 2016. Multiphysics Simulation of Infrared Signature of an Ice Cube. *The International Journal of Multiphysics,* 10.

LOZOWSKI E.P, S. K., MAKKONEN L. 2000. Computer simulation of marine ice accretion. *Philos Trans R Soc A***,** 811–2845.

MAKKONEN, L. 1984. Atmospheric icing on sea structures. Hanover, (NH): US Army Cold Regions Research and Engineering Laboratory.

MORAN, M. J. 2003. *Introduction to thermal systems engineering: thermodynamics, fluid mechanics, and heat transfer,* Wiley.

OVERLAND, J., PEASE, C., PREISENDORFER, R. & COMISKEY, A. 1986. Prediction of vessel icing. *Journal of climate and applied meteorology,* 25**,** 1793-1806.

RASHID, T., KHAWAJA, H. A. & EDVARDSEN, K. 2016a. Ice Detection of Pure and Saline Ice Using Infrared Signature. *Sensors & Transducers,* 206**,** 82.

RASHID, T., KHAWAJA, H. A. & EDVARDSEN, K. 2016b. Review of marine icing and anti-/de-icing systems. *Journal of Marine Engineering & Technology,* 15**,** 79-87.

RASHID, T., KHAWAJA, H. A., EDVARDSEN, K. & MUGHAL, U. N. 2015. Infrared thermal signature evaluation of a pure and saline ice for marine operations in cold climate. *Sensors & Transducers,* 194**,** 62.

ROEBBER, P. & MITTEN, P. 1987. Modelling and measurement of icing in Canadian waters. Downsview, Ontario: Canadian Climate Centre.

RYERSON, C. C. 2009. Assessment of superstructure ice protection as applied to offshore oil operations safety. Hanover (NH): US Army Corps of Engineers.

RYERSON, C. C. 2011. Ice protection of offshore platforms. *Cold Regions Science and Technology,* 65**,** 97-110.

SAMUELSEN, E. M., EDVARDSEN, K. & GRAVERSEN, R. G. 2017. Modelled and observed sea-spray icing in Arctic-Norwegian waters. *Cold Regions Science and Technology,* 134**,** 54-81.

SHEA, C. & JAMIESON, B. 2011. Some fundamentals of handheld snow surface thermography. *The Cryosphere,* 5**,** 55.

SHELLARD, H. C. 1974. The Meteorological Aspects of Ice Accretion on Ships. *Marine Science Affairs* Geneva: World Meteorological Organization.

STALLABRASS, J. 1980. Trawler Icing. A Compilation of Work Done at N.R.C. Ottawa, Canada.

SULTANA, K. R., DEHGHANI, S. R., POPE, K. & MUZYCHKA, Y. S. 2018. A review of numerical modelling techniques for marine icing applications. *Cold Regions Science and Technology,* 145**,** 40-51.

WMO 1962. Precipitation Measurements at Sea. Geneva: World Meteorological Organization.

ZAKRZEWSKI, W., LOZOWSKI, E. & HORJEN, I. The use of ship icing models for forecasting icing rates on sea-going ships. Pro. 10th Int'l. Conf. on Port and Ocean Engineering under Arctic Conditions, 1989. Luleå University of Technology, 1454-1467.

ZHANG, Y. 1999. *MODIS (Moderate Resolution Imaging Spectrometer), USCB Emissivity Library* [Online]. USCB Emissivity Library. Available: https://icess.eri.ucsb.edu/modis/EMIS/html/em.html [Accessed].

Graphical abstract

Heat energy is supplied to an ice sample for a certain period inside a cold environment. The surface temperature of the sample is monitored during this period using an infrared camera. Three ice samples' thicknesses are selected for comparison (5mm, 10mm and 15mm). Results show that time to respond (t_0), rate of change of temperature $\left(\frac{\partial T}{\partial t}\right)$, and time to reach ΔT of 5^{o}C (t_f) can be empirically correlated to initial temperature (T_0) and ice thickness (t_h). It was found that time to respond (t_0) had a strong correlation with ice thickness (t_h).

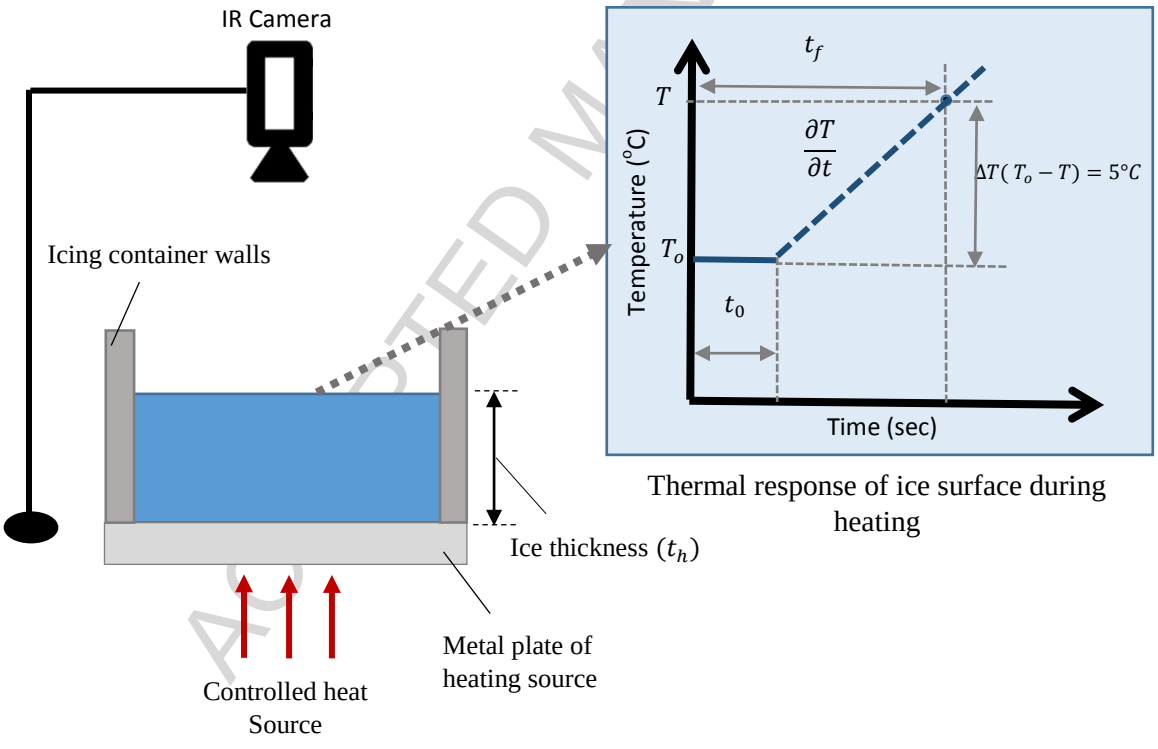

Thermal response of ice surface during heating

Highlights

- Marine icing is one of key challenge for operating in a cold climate, and its mitigation is vital for marine operations.
- In given study, infrared thermography (IRT) is used to measure the thermal response of marine ice when subjected to active heating.
- Given tests are performed at various controlled climatic conditions for three different ice thicknesses (5, 10 and 15mm).
- The IRT thermal profile revealed three parameters, namely: time to respond (t_0), rate of change of temperature $\left(\frac{\partial T}{\partial t}\right)$, and time to reach ΔT of 5^{o}C (t_f).
- It was found that time to respond (t_0) had a strong correlation with ice thickness (t_h).